HOKKAIDO UNIVERSITY

Title	Healing Sulfur Vacancies in Monolayer MoS2 by High-Pressure Sulfur and Selenium Annealing: Implication for High-Performance Transistors
Author(s)	Yanase, Takashi; Uehara, Fumiya; Naito, Itsuki et al.
Citation	ACS Applied Nano Materials, 3(10), 10462-10469 https://doi.org/10.1021/acsanm.0c02385
Issue Date	2020-10-23
Doc URL	https://hdl.handle.net/2115/83045
Rights	This document is the Accepted Manuscript version of a Published Work that appeared in final form in ACS Applied Nano Materials, copyright c American Chemical Society after peer review and technical editing by the publisher. To access the final edited and published work see http://doi.org/10.1021/acsanm.0c02385.
Type	journal article
File Information	Manuscript ver.pdf

Hokkaido University Collection of Scholarly and Academic Papers : HUSCAP

Healing Sulfur Vacancies in Monolayer MoS_2 by High-Pressure Sulfur and Selenium Annealing

Takashi Yanase*, Fumiya Uehara, Itsuki Naito, Taro Nagahama, Toshihiro Shimada

Division of Applied Chemistry, Faculty of Engineering, Hokkaido University, Kita 13 Nishi 8 Kita-ku, Sapporo 060-8628, Japan

*Corresponding author: Takashi Yanase

Email address: yanase42@eng.hokudai.ac.jp (T. Y.)

ABSTRACT

Developing a technology to terminate chalcogen vacancies for transition metal dichalcogenides is a crucial task for applications, such as diodes, transistors, and sensors, because chalcogen vacancies degrade the electronic and optical properties. This article reports a healing method of S vacancies in MoS_2 by high-pressure annealing under 5 atm of S vapor pressure. The crystal quality after a mechanical transfer, S annealing, and vacuum annealing was systematically studied by observing the photoluminescence (PL). The remarkable recovery of the A exciton emission peak in the PL spectrum indicated repair of the crystal quality in MoS_2 by the S annealing. We also demonstrated that the S vacancies could be terminated by Se atoms using a high-pressure annealing

method. The crystal quality of $MoS_{2(1-x)}Se_{2x}$ alloy was confirmed by transmission electron microscopy and electron diffraction.

KEYWORDS: high-pressure annealing, MoS_2, S vacancies, photoluminescence, chemical vapor deposition, monolayer

After the scotch tape method was established to make graphene from graphite,[1]many other layered materials have attracted much attention in the past decade.[2–7] Particularly, semiconducting transition metal dichalcogenides (TMDCs), such as MoS_2,[8,9] $MoSe_2$,[10] WS_2,[11–13] and HfS_2,[14–16] have been widely studied due to the unique electronic and optical properties derived from the non-zero bandgap unlike graphene. The non-zero bandgap is a crucial feature for practical applications such as digital circuits and low-power-consumption electronics.

Although the scotch tape method is still used for the fundamental science of layered materials, chemical vapor deposition (CVD) is one of the best methods to make high-quality monolayer TMDCs on a wafer-scale. Due to the recent progress of CVD,[17–19] the crystal quality of MoS_2 grown on sapphire is comparable to that of exfoliated MoS_2. Since the crystal quality governs the electronic and optical properties, such as carrier mobility[20,21] and the intensity of the photoluminescence (PL),[20,22,23] it is vital to maintain the crystal quality during the device fabrication process, for example, microscopic peeling off from the original substrate, mechanical transfer to another substrate, and lithography for microfabrication. However, the chemical wet process during mechanical transfer may cause damage to the MoS_2 due to the relatively weak bond between the Mo and S. In other words, the formation of S vacancies and oxidation easily occur

during the mechanical transfer. Therefore, it is crucial to establish a defect healing technology for high-performance transistors,[8,24] photovoltaics,[25] and phototransistors.[26] While the dipping in a thiol solution (thiol healing) was suggested as a simple defect healing method in 2012,[24,27,28] several researchers insisted that thiol molecules were merely physisorbed on the MoS_2.[29] The inconsistent conclusions of the thiol healing are probably because the property of MoS_2 is sensitive to the small number of S vacancies (even less than 1%), and it is difficult to detect them in the monolayer MoS_2. Thermal annealing is another healing technology to improve the structural order and release the stress. However, the thermal annealing under argon, oxygen, and vacuum resulted in non-stoichiometric MoS_2 due to the volatility of the S atoms.[30–32] In order to resolve these issues, an alternative defect healing method should be established.

In this study, a high-pressure S annealing method was proposed as a defect healing method. A high-quality MoS_2 as the standard material was synthesized on sapphire by CVD because it is well-known that the monolayer MoS_2 grown on sapphire has the best quality due to its epitaxial growth.[17,18] The MoS_2 grown on the sapphire was transferred to a SiO_2/Si substrate to investigate the influence on the quality of the monolayer MoS_2. The defective transferred monolayer MoS_2 was annealed under 5 atm of S vapor pressure to heal the S vacancies. Vacuum annealing was also carried out to examine the variation in the crystal quality. The change in crystal quality was systematically studied by observing the PL that is sensitive to the defects to determine how the mechanical transfer, high-pressure S annealing, vacuum annealing affects the crystal quality. Se annealing was conducted to investigate whether Se atoms cure the S vacancies, which can be used to make an $MoS_{2(1-x)}Se_2$ alloy by post annealing.

RESULTS AND DISCUSSION

Monolayer MoS_2 was grown on sapphire based on the gas-phase reaction of MoO_3 and S vapor using a specially designed separate-flow-system CVD. The detailed growth procedure is described in the METHODS section and supplementary information. Figures 1(a) show an optical microscopic (OM) image of the triangular monolayer MoS_2 with a single-crystal domain on sapphire. The two distinctive crystallographical orientations of the MoS_2 domains can be seen in the OM image and interpreted as the epitaxial growth due to the lattice match.[7] The orientation histogram shown in Fig. 1(b) illustrates that most of the single triangle domains are oriented to 0° or $\pm 60^{o}$, which is consistent with the previously reported epitaxial MoS_2 monolayer.[33] Since the in-plane lattice constant of sapphire (0.476 nm) is approximately 1.5 times greater than that of MoS_2 (0.315 nm), a 3×3 structure of the MoS_2 fits on a 2×2 structure of the sapphire as shown in Fig. S1.[18] While the MoS_2 grown on the sapphire showed a nearly perfect triangle domain and high orientation, the distorted triangle and randomly oriented MoS_2 formed on the SiO_2/Si is shown in Fig. S2. The highly-oriented domains indicated that the quality of the MoS_2 monolayer on the sapphire was superior to that on the SiO_2/Si. The thickness uniformity of MoS_2 grown on sapphire was observed by the homogeneous color contrast of the triangle domains as seen in Fig. 1(a). Furthermore, the height of the MoS_2 domains was measured to be 0.65 nm by AFM as seen in Figs. 1(c) and (d), which agrees well with the previously reported thickness of the monolayer MoS_2.[19,34,35]

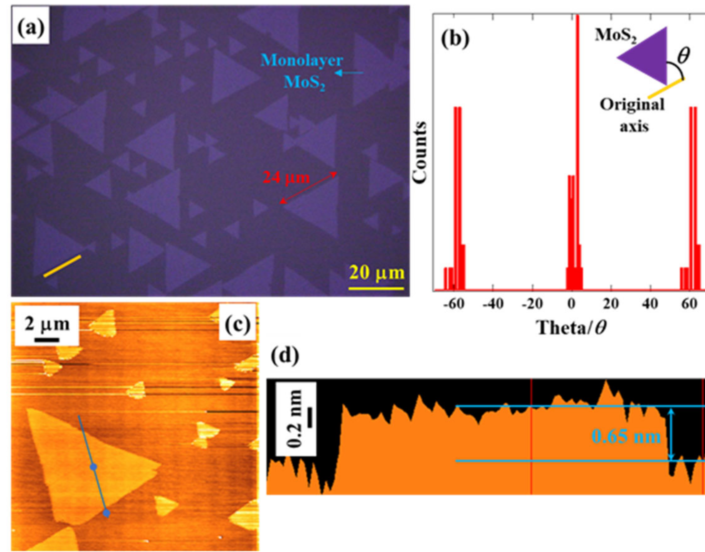

Figure 1. (a) Microscopic image of monolayer MoS_2 grown on sapphire. The orange bar is the original axis (0°) used to measure the orientation angles (theta) to make the histogram shown in (b). (b) An orientation histogram of MoS_2 monolayer to illustrate the epitaxy between MoS_2 and sapphire. The inset shows the geometrical relationship between the original axis and MoS_2 to measure theta. (c) An AFM image of monolayer MoS_2. (d) Line profile at the blue line in (c) to show the thickness of the MoS_2 monolayer (0.65 nm).

We further confirmed the quality of the triangle-domain single-crystal monolayer MoS_2 by obtaining Raman and photoluminescent (PL) spectra as shown in Figs. 2(a) and (b), respectively. The Raman and PL spectra of the MoS_2 monolayer grown on the SiO_2/Si substrate are also shown for comparison. Two characteristic peaks of E^1_{2g} at 385.6 cm-^{1} and A_{1g} 405.7 cm^{-1} in the Raman spectra represent the in-plane vibrational mode and out-of-plane vibrational mode of MoS_2, respectively. The shoulder peak at 415.0 cm^{-1} was ascribed to the sapphire. The frequency difference between the E^1_{2g} and A_{1g} peaks (20.1 cm^{-1}) is close to the reported value of the

monolayer MoS_2.[18,36] The crystal quality of the MoS_2 monolayer on the sapphire was better than that on the SiO_2/Si because the full width at half maximum (FWHM) of the A_{1g} peak for the MoS_2 grown on the sapphire (5.43cm^{-1}) was narrower than that on the SiO_2/Si (9.52cm^{-1}). The intensity of the Raman spectra in Fig. 2(a) was scaled to compare the FWHM. The PL spectrum (Fig. 2(b)) shows the strong A excitonic peak located at 655 nm (1.81 eV) while the negligible B excitonic peak (616 nm) was observed. The sharp peak located at 694 nm originated from the sapphire. The narrow FWHM (~25 nm) and intense A excitonic peak indicated the significant optical quality and few defects in the monolayer MoS_2 because the PL spectra, especially the intensity of the A excitonic peak, is sensitive to the crystal quality.[21,23] The broader and less intense PL peak of MoS_2 grown on the SiO_2/Si were probably due to the defects of the S vacancies, the charge traps on the SiO_2 surface, and the distortion of the MoS_2 structure. The chemical compositions of the monolayer MoS_2 grown on the sapphire and SiO_2/Si were determined to be 1:2.02 and 1:1.79, respectively, by XPS (Fig. S3). The Mo/S ratios are consistent with the result of the OM image, Raman, and PL spectrum that show few S vacancies exist in the MoS_2 grown on the sapphire while there were some S vacancies in that grown on SiO_2/Si.

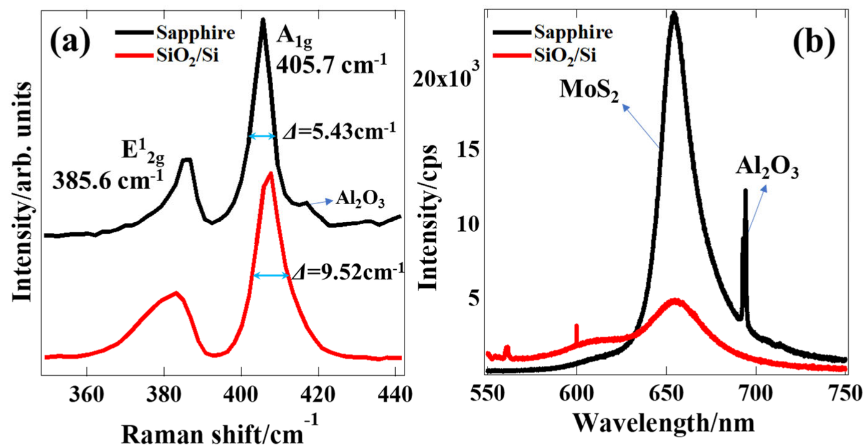

Figure 2. (a) Raman spectrum of monolayer MoS_2 grown on sapphire (black) and SiO_2/Si (red). Two distinctive vibrational modes of E^1_{2g} and A_{1g} illustrate the formation of MoS_2. The crystal quality of MoS_2 grown on the sapphire was superior to that on SiO_2/Si because of the narrower FWHM. (b) PL spectrum of monolayer MoS_2 grown on the sapphire (black) and SiO_2/Si (red). The strong A exciton emission peak indicates the high crystal quality of MoS_2 on the sapphire.

MoS_2 grown on the sapphire was used as a standard sample to investigate how the mechanical transfer, S annealing, and vacuum annealing affect the quality of the monolayer MoS_2 because the defect formation and healing can be detected by observing the PL.[37] Each step of mechanical transfer, S annealing, and vacuum annealing was carried out as follows. First, the monolayer MoS_2 grown on the sapphire was transferred onto a SiO_2/Si substrate by the chemical wet process according to Ref. 38. Next, the transferred MoS_2 was annealed in a sealed quartz tube at 800 ºC for 30 min under 5 atm of S vapor pressure that was estimated by the ideal gas equation ($pV=nRT$). Lastly, the sample was annealed under a vacuum of 10^{-3} Pa at 800 ºC for 30 min. The detailed procedures of the mechanical transfer and S annealing are described in the METHODS section and supplementary information. Figure 3 shows the PL spectra of MoS_2 (i) grown on sapphire, (ii) transferred on SiO_2/Si, (iii) annealed in the S atmosphere, and (iv) annealed under vacuum. Broadening the peak and lowering the intensity of PL for the transferred MoS_2 illustrate that strain or/and defects were induced in the lattice because a pronounced peak located at 655 nm from the A exciton is easily quenched by strain and defects. The recovery of the peak sharpness implies that the strain or defects was healed by the S annealing. Vacuum annealing introduced many defects (S vacancies) again, resulting in lowering the intensity.

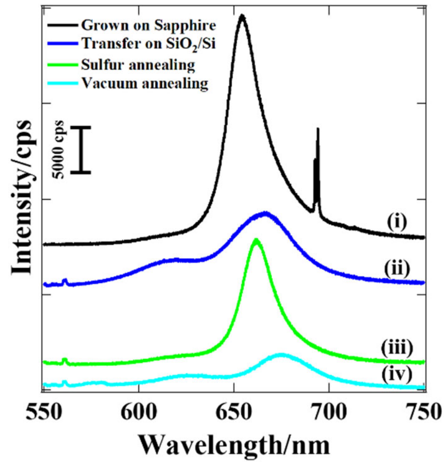

Figure 3. PL spectra of MoS_2 (i) grown on sapphire (ii) transferred on SiO_2/Si (iii) annealed under 5 atm of S vapor pressure (iv) annealed under vacuum. The peak intensity of the A exciton shows the crystal quality of MoS_2.

In order to quantitatively analyze the PL spectra, each spectrum was deconvoluted with three or four emission peaks (Gaussian-Lorentzian function) including the A exciton peak. Each emission peak was labeled by X_A, X_B, X^-, and X_{be} as shown in Figs. 4(a)-(d). All the spectra were scaled to compare the results of the deconvolution. The sapphire peak located at 695 nm in Fig. 4(a) was removed to obtain a good fitting curve. X_A is the neutral A excitons as already mentioned, which is associated with direct optical transitions from the valence band to the conduction band. The emission peak at 616 nm (X_B) is due to the spin split of the valance band at the K-valley. The other emission peak at 678 nm (X^-) is derived from a trion which is a bound state of one exciton and one electron, in other words, a negatively-charged exciton. The weakest peak at 698 nm (X_{be}) appeared after the mechanical transfer is assignable to the bound excitons (X_{be}) that are neutral excitons bound to defects such as S vacancies. The spectral contributions from the four kinds of excitons are understandable by the schematic band diagram shown in Fig. 4(e).[37,39] Figure 4(f) shows the

variation of the individual spectral contribution obtained from the deconvoluted curves and total intensity of the PL spectra. It should be noted that the X_A is sensitive to the carrier density because the excessive carrier is bound to the excitons (formation of trion), resulting in a quenching of PL from X_A.[39,40] Since the S vacancies emit two extra electrons, the X_A peak strongly depends on the number of S vacancies. Besides, X_{be} can be used to estimate the defect density (S vacancies)[37] while X_B and X^- were hardly used to discuss the MoS_2 quality. The PL spectra of the as-grown sample on the sapphire (Fig. 4(a)) has a significant contribution from the X_A exciton and no contribution from the X_{be} exciton due to the high crystal quality (defect-free). Mechanical transfer of the MoS_2 onto a SiO_2/Si induced the defects, such as S vacancies, because the X_A peak decreased and X_{be} peak appeared (Fig. 4(b)). The chemical wet process during mechanical transfer may cause damage such as oxidation, wrinkles, and formation of S vacancies. The broad peak also indicates the disorder of the MoS_2 crystal structure. High-pressure annealing in the S atmosphere (Fig. 4(c)) recovered the crystal quality since the contribution of X_A returned to nearly the original value and the spectrum can be fitted without the X_{be} peak. However, the incomplete recovery of the total intensity implies that the influence of charge traps on SiO_2 and charge transfer from SiO_2 could not be eliminated by S annealing. These effects can be removed by using hexagonal boron nitride as the substrate.[9] Vacuum annealing (Fig. 4(d)) drastically induced the S vacancies due to the volatility of the S atoms. A decrease in the total intensity shows the increase in the nonradiative recombination rate due to the defect states.

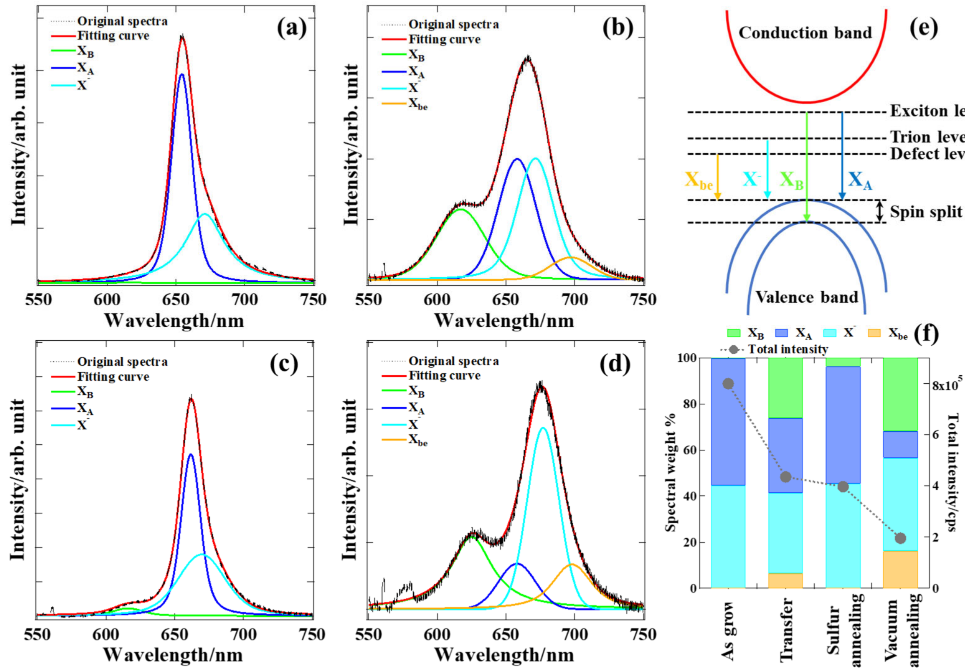

Figure 4. The deconvolution of PL spectra of MoS_2 (a) grown on sapphire (b) transferred on SiO_2/Si (c) annealed under 5 atm of S vapor pressure (d) annealed under vacuum. (e) Schematic band diagram of MoS_2 and four emissive transitions that were used to deconvolute the PL spectra. (f) The variation in the spectral weight and total intensity after each step.

If the S vacancies can be repaired by different chalcogenides, such as Se, it is useful to optimize the electric properties after the MoS_2 growth. Therefore, the $MoS_{2(1-x)}Se_{2x}$ alloy was made by post-annealing under a Se atmosphere in a quartz tube (the same pressure and temperature as the S annealing) using the defective MoS_2 created by vacuum annealing. The formation of $MoS_{2(1-x)}Se_{2x}$ was confirmed by its Raman and PL spectra as shown in Fig. 5. The Raman and PL spectra of the transferred and vacuum annealed samples are also shown for comparison. The Raman spectrum shows that the Se-Mo vibrational modes (A_{1g} and E_{2g}) located at 282 and 302 cm^{-1} were observed after the Se annealing while only the S-Mo modes were seen before the Se annealing. There still remained two peaks of MoS_2 located at 380 cm^{-1} (E_{2g}(S-Mo)) and 405 cm^{-1} (A_{1g}(S-Mo)) even after

the Se annealing. The peak position of the E_{2g}(S-Mo) vibrational mode shifted to a lower frequency because the S-Mo bonding would be softened by the incorporation of the heavy Se atoms, which is consistent with the previous reports.[41,42] It has already been reported that the A_{1g}(S-Mo) was not significantly affected by the introduction of Se.[41,42] The Se annealing was also carried out for the as-grown sample (without vacuum annealing) as shown in Fig. S4. Although a small A_{1g} peak was observed due to the S/Se exchange reaction, the two-step annealing (vacuum annealing and Se annealing) was more efficient to incorporate Se atoms into the MoS_2.

Figure 5(b) shows the PL spectra of the transferred sample, vacuum-annealed sample, and Se annealed sample. The emission peak from the exciton (X_A) was red-shifted because the bandgap would become narrower due to the alloying with Se. The Se molar fraction was estimated from the center of the emission peak to be approximately 10%[41]. Non-recovery of the PL intensity did not mean many S vacancies remained (poor crystal quality) because the introduction of Se atoms quenches the PL[41].

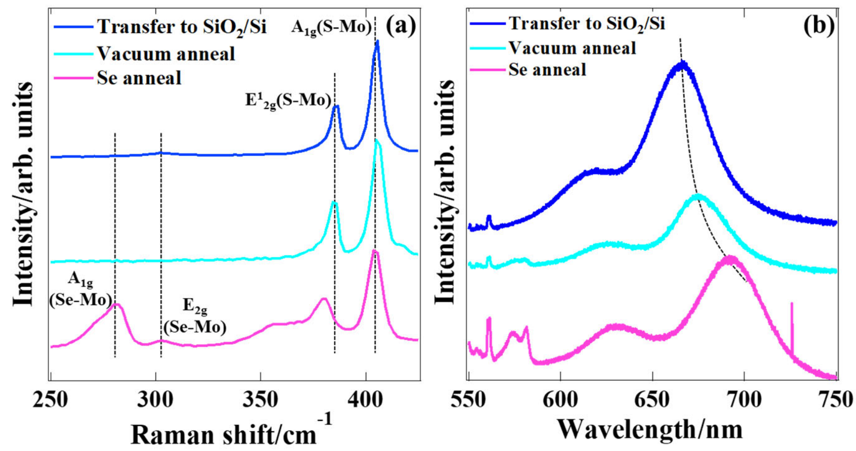

Figure 5. (a) Raman spectra of MoS_2 transferred to SiO_2/Si, annealed under vacuum, and annealed in Se atmosphere. Two peaks located at 282 and 302 cm^{-1} correspond to the Se-Mo

vibrational modes. (b) PL spectra of MoS_2 transferred to SiO_2/Si, annealed under vacuum, and annealed in Se atmosphere. The red shift of peak top shows the bandgap shrinkage due to the alloying with Se.

A TEM image and electron diffraction were acquired to confirm the crystal quality of $MoS_{2(1-x)}Se_{2x}$ as shown in Figs. 6(a) and (b). The TEM-EDS indicates the inclusion of Se atoms after the Se annealing as shown in Fig. S5. The edge angle of the crystal (118°) reflects the hexagonal crystal system of $MoS_{2(1-x)}Se_{2x}$. Electron diffraction from the area marked with a blue circle in Fig. 6(a) revealed that the nanosheet of $MoS_{2(1-x)}Se_{2x}$ was a single-crystal hexagonal structure. The *d* value calculated from a line profile (Fig. 6(c)) of the <100> direction (yellow line in Fig. (b)) was 0.271 nm which is good agreement with the previously reported (100) plane spacing of $MoS_{2(1-x)}Se_{2x}$ with the same composition ratio (10% Se)[41].

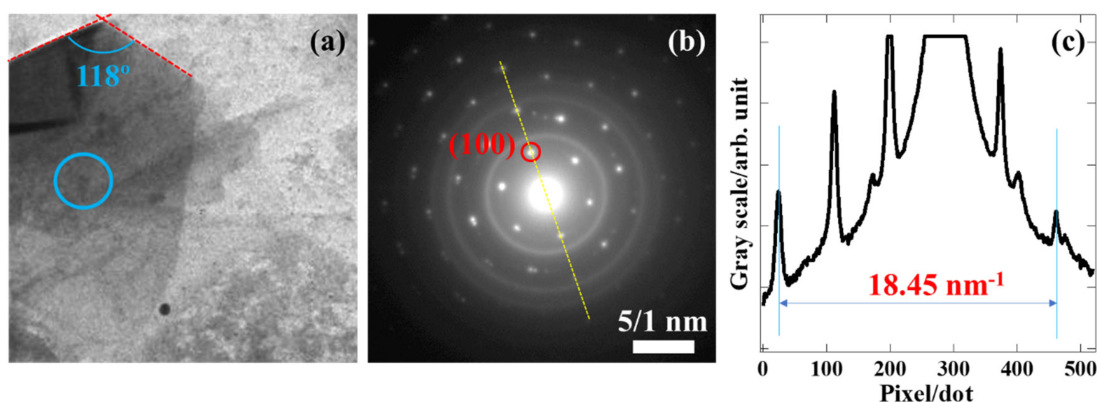

Figure 6. (a) TEM image of $MoS_{2(1-x)}Se_{2x}$ after high-pressure annealing under Se atmosphere. (b) Electron diffraction of $MoS_{2(1-x)}Se_{2x}$ obtained from the area marked with the blue circle in (a). (c) A line profile of the yellow line in (b) to calculate the *d* value of (100).

CONCLUSIONS

The influence of mechanical transfer, S annealing, vacuum annealing, and Se annealing on the monolayer MoS_2 was systematically studied by observing the PL spectra. Even though the mechanical transfer damaged the MoS_2, it can be repaired by high-pressure annealing under 5 atm of S vapor pressure. In addition, the S vacancies created by vacuum annealing were terminated with the Se atoms by high-pressure annealing. The post-annealing at elevated temperature can be used to heal the defects and modulate the composition ratio of the TMDCs, which could be an essential technique to fabricate practical electronic and optoelectronic devices.

METHODS

Growth procedure of monolayer MoS_2. The monolayer MoS_2 was synthesized by an atmospheric pressure CVD (APCVD) with a separate-flow system. The detailed geometry of our APCVD is shown in Fig. S6.[7,43,44] In this system, we can separately control the temperatures of MoO_3, S, and substrate as well as flow rates of the MoO_3 and S lines to guarantee the controllability and reproducibility. MoO_3 (Kanto Chemical Co., Inc. >99.5%) and S (Kanto Chemical Co., Inc. >99.5%) powders were utilized as the source materials without further purification. 5 × 5 mm^2 sapphire (c-plane) and 1 × 1 cm^2 SiO_2(285 nm)/Si wafers were used as the substrates. The sapphire and SiO_2/Si were cleaned by the RCA (Radio Corporation of America) cleaning method[45] to remove any metal and organic contaminants. The sapphire was annealed in air for 1 hour at 1000 ºC, which is a key to make the atomically smooth oriented MoS_2 monolayer.[18,33] After the introduction of the substrate in a quartz tube, the system was purged with Ar. The temperatures of the MoO_3, S, and substrates increased to the set points while keeping the flow through the S line in order not have air enter the quartz tube. When the temperatures reached the set points, the Ar

flow through the MoO_3 line was set to 150 sccm to start the MoS_2 growth. The growth time was defined as the duration of Ar flowing through the MoO_3 line. After the growth of the MoS_2 monolayer, the furnace was naturally cooled while the S supply was maintained until the temperature of the substrate had decreased to 350 ºC in order for the MoS_2 not to be oxidized. The reaction conditions of the temperatures, flow rates, and reaction time to make the monolayer MoS_2 are summarized at the bottom of Fig. S6.

Characterization of $MoS_2/MoS_{2(1-x)}Se_{2x}$. The morphology of the monolayer MoS_2 on the substrate was observed by an optical microscope (OM, OM mode of a laser microscope, VK-8710) and an atomic force microscope (AFM, SII SPI-3800). The quality of the monolayer MoS_2 was confirmed by Raman and PL spectroscopies (Reinshaw Invia) with 532 nm laser excitation. The chemical composition was measured by X-ray photoelectron spectroscopy (XPS, JPS-9200). The morphology and crystallinity of the $MoS_{2(1-x)}Se_{2x}$ alloy were confirmed by transmission electron microscopy and electron diffraction(TEM, JEM-2010).

Mechanical transfer of the monolayer MoS_2 onto a SiO_2/Si substrate. A 1.0 wt% PMMA dichloromethane (DCM) solution was spin-coated on a monolayer MoS_2 grown on sapphire at a speed of 3000 rpm for 60 seconds. A polydimethylsiloxane (PDMS) film was placed on the sapphire substrate, then the substrate was cooled at 2 ºC in a refrigerator. The surface of a SiO_2/Si was fluorinated under vacuum with a drop of trichloro(1H,1H,2H,2H-perfluorooctyl)silane for 12 hours. A mixture of PDMS and curative with a ratio of 10:1 was spin-coated at the speed of 1250 rpm for 30 sec, then the wafer was dried in an oven at 80 ºC. The PDMS/PMMA/MoS_2 film was peeled off from the sapphire and transferred onto the fluorinated SiO_2/Si. Only the PDMS film could be removed by warming the SiO_2/Si wafer at 110 ºC because the adhesion between the

PDMS and PMMA/MoS_2 weakened. The PMMA was washed away with DCM, then the SiO_2/Si was dried using a nitrogen gun.

Sulfur/selenium annealing. The MoS_2 (on substrate) was sealed in a quartz tube with S (Se) powder under a vacuum of 1.0×10^{-3} Pa. In order to avoid direct contact between the MoS_2 and S (Se), the substrate was located at the center of the quartz tube. The amount of S (Se) powder was calculated by the ideal gas equation to reach 5 atm of S (Se) vapor pressure. The quartz tube was annealed in a furnace at 800 ºC for 30 min. The schematic illustration of the procedure is depicted in Fig. S7.

Vacuum annealing. The MoS_2 was sealed in a quartz tube under a vacuum of 1×10^{-3} Pa. The MoS_2 was placed in a furnace at 800 ºC for 30 min. It should be noted that complete removal of air (oxygen) was critical to making adequate S vacancies because the oxidation or etching of MoS_2 occurred when it was higher than 5 Pa.

AUTHOR INFORMATION

Corresponding Author

*Takashi Yanase

Email address: yanase42@eng.hokudai.ac.jp

Author Contributions

The manuscript was written with contributions by all the authors. All the authors have given approval to the final version of the manuscript. ‡These authors equally contributed.

Funding Sources

This research was partially supported by KAKENHI 17H03380 from MEXT Japan.

ACKNOWLEDGMENT

Instrumental analyses were supported by the Nanotechnology platform at Hokkaido University by METI, Japan.

ASSOCIATED CONTENT

The Supporting Information is available free of charge on the ACS Publication website at DOI:

REFERENCES

(1) Novoselov, K. S.; Geim, A. K.; Morozov, S. V; Jiang, D.; Zhang, Y.; Dubonos, S. V.; Grigorieva, I. v; Firsov, A. A. Electric Field Effect in Atomically Thin Carbon Films Supplementary. *Science* **2004**, *5*, 1–12. https://doi.org/10.1126/science.aab1343.

(2) Geim, A. K.; Grigorieva, I. V. Van Der Waals Heterostructures. *Nature* **2013**, *499*, 419–425. https://doi.org/10.1038/nature12385.

(3) Wang, H.; Huang, X.; Lin, J.; Cui, J.; Chen, Y.; Zhu, C.; Liu, F.; Zeng, Q.; Zhou, J.; Yu, P.; *et al.* High-Quality Monolayer Superconductor $NbSe_2$ Grown by Chemical Vapour Deposition. *Nat. Commun.* **2017**, *8*, 1–8. https://doi.org/10.1038/s41467-017-00427-5.

(4) Kim, S. M.; Hsu, A.; Park, M. H.; Chae, S. H.; Yun, S. J.; Lee, J. S.; Cho, D. H.; Fang, W.; Lee, C.; Palacios, T.; *et al.* Synthesis of Large-Area Multilayer Hexagonal Boron Nitride for High Material Performance. *Nat. Commun.* **2015**, *6*. https://doi.org/10.1038/ncomms9662.

(5) Kim, K. K.; Hsu, A.; Jia, X.; Kim, S. M.; Shi, Y.; Hofmann, M.; Nezich, D.; Rodriguez-Nieva, J. F.; Dresselhaus, M.; Palacios, T.; *et al.* Synthesis of Monolayer Hexagonal Boron Nitride on Cu Foil Using Chemical Vapor Deposition. *Nano Lett.* **2012**, *12*, 161–166. https://doi.org/10.1021/nl203249a.

(6) Wang, L.; Wu, B.; Jiang, L.; Chen, J.; Li, Y.; Guo, W.; Hu, P.; Liu, Y. Growth and Etching of Monolayer Hexagonal Boron Nitride. *Adv. Mater.* **2015**, *27*, 4858–4864. https://doi.org/10.1002/adma.201501166.

(7) Yanase, T.; Watanabe, S.; Weng, M.; Wakeshima, M.; Hinatsu, Y.; Nagahama, T.; Shimada, T. Chemical Vapor Deposition of NbS_2 from a Chloride Source with H_2 Flow: Orientation Control of Ultrathin Crystals Directly Grown on SiO_2 /Si Substrate and Charge Density Wave Transition. *Cryst. Growth Des.* **2016**, *16*, 4467–4472. https://doi.org/10.1021/acs.cgd.6b00601.

(8) Lembke, D.; Kis, A. Breakdown of High-Performance Monolayer MoS_2 Transistors. *ACS Nano* **2012**, *6*, 10070–10075. https://doi.org/10.1021/nn303772b.

(9) Wang, S.; Wang, X.; Warner, J. H. All Chemical Vapor Deposition Growth of MoS_2:H-BN Vertical van Der Waals Heterostructures. *ACS Nano* **2015**, *9*, 5246–5254. https://doi.org/10.1021/acsnano.5b00655.

(10) Kong, D.; Wang, H.; Cha, J. J.; Pasta, M.; Koski, K. J.; Yao, J.; Cui, Y. Synthesis of MoS_2 and $MoSe_2$ Films with Vertically Aligned Layers. *Nano Lett.* **2013**, *13*, 1341–1347. https://doi.org/10.1021/nl400258t.

(11) Behura, S.; Nguyen, P.; Che, S.; Debbarma, R.; Berry, V. Large-Area, Transfer-Free, Oxide-Assisted Synthesis of Hexagonal Boron Nitride Films and Their Heterostructures with MoS_2 and WS_2. *J. Am. Chem. Soc.* **2015**, *137*, 13060–13065. https://doi.org/10.1021/jacs.5b07739.

(12) Hill, H. M.; Rigosi, A. F.; Roquelet, C.; Chernikov, A.; Berkelbach, T. C.; Reichman, D. R.; Hybertsen, M. S.; Brus, L. E.; Heinz, T. F. Observation of Excitonic Rydberg States in Monolayer MoS_2 and WS_2 by Photoluminescence Excitation Spectroscopy. *Nano Lett.* **2015**, *15*, 2992–2997. https://doi.org/10.1021/nl504868p.

(13) Li, C.; Kameyama, T.; Takahashi, T.; Kaneko, T.; Kato, T. Nucleation Dynamics of Single Crystal WS_2 from Droplet Precursors Uncovered by In-Situ Monitoring. *Sci. Rep.* **2019**, *9*, 1–7. https://doi.org/10.1038/s41598-019-49113-0.

(14) Yan, C.; Gan, L.; Zhou, X.; Guo, J.; Huang, W.; Huang, J.; Jin, B.; Xiong, J.; Zhai, T.; Li, Y. Space-Confined Chemical Vapor Deposition Synthesis of Ultrathin HfS_2 Flakes for Optoelectronic Application. *Adv. Funct. Mater.* **2017**, *27*, 1–9. https://doi.org/10.1002/adfm.201702918.

(15) Fu, L.; Wang, F.; Wu, B.; Wu, N.; Huang, W.; Wang, H.; Jin, C.; Zhuang, L.; He, J.; Fu, L.; *et al.* Van Der Waals Epitaxial Growth of Atomic Layered HfS_2 Crystals for Ultrasensitive Near-Infrared Phototransistors. *Adv. Mater.* **2017**, *29*, 1–8. https://doi.org/10.1002/adma.201700439.

(16) Kanazawa, T.; Amemiya, T.; Ishikawa, A.; Upadhyaya, V.; Tsuruta, K.; Tanaka, T.; Miyamoto, Y. Few-Layer HfS_2 Transistors. *Sci. Rep.* **2016**, *6*, 1–9. https://doi.org/10.1038/srep22277.

(17) Dumcenco, D.; Ovchinnikov, D.; Marinov, K.; Lazić, P.; Gibertini, M.; Marzari, N.; Sanchez, O. L.; Kung, Y. C.; Krasnozhon, D.; Chen, M. W.; *et al.* Large-Area Epitaxial Monolayer MoS_2. *ACS Nano* **2015**, *9*, 4611–4620. https://doi.org/10.1021/acsnano.5b01281.

(18) Ji, Q.; Kan, M.; Zhang, Y.; Guo, Y.; Ma, D.; Shi, J.; Sun, Q.; Chen, Q.; Zhang, Y.; Liu, Z. Unravelling Orientation Distribution and Merging Behavior of Monolayer MoS_2 Domains on Sapphire. *Nano Lett.* **2015**, *15*, 198–205. https://doi.org/10.1021/nl503373x.

(19) Chen, W.; Zhao, J.; Zhang, J.; Gu, L.; Yang, Z.; Li, X.; Yu, H.; Zhu, X.; Yang, R.; Shi, D.; *et al.* Oxygen-Assisted Chemical Vapor Deposition Growth of Large Single-Crystal and High-Quality Monolayer MoS_2. *J. Am. Chem. Soc.* **2015**, *137*, 15632–15635. https://doi.org/10.1021/jacs.5b10519.

(20) Yu, Z.; Pan, Y.; Shen, Y.; Wang, Z.; Ong, Z. Y.; Xu, T.; Xin, R.; Pan, L.; Wang, B.; Sun, L.; *et al.* Towards Intrinsic Charge Transport in Monolayer Molybdenum Disulfide by Defect and Interface Engineering. *Nature Commun.* **2014**, *5*, 1–7. https://doi.org/10.1038/ncomms6290.

(21) Kim, I. S.; Sangwan, V. K.; Jariwala, D.; Wood, J. D.; Park, S.; Chen, K. S.; Shi, F.; Ruiz-Zepeda, F.; Ponce, A.; Jose-Yacaman, M.; et al. Influence of Stoichiometry on the Optical and Electrical Properties of Chemical Vapor Deposition Derived MoS_2. *ACS Nano* **2014**, *8*, 10551–10558. https://doi.org/10.1021/nn503988x.

(22) Nan, H.; Wang, Z.; Wang, W.; Liang, Z.; Lu, Y.; Chen, Q.; He, D.; Tan, P.; Miao, F.; Wang, X.; *et al.* Strong Photoluminescence Enhancement of MoS_2 through Defect

Engineering and Oxygen Bonding. *ACS Nano* **2014**, *8*, 5738–5745. https://doi.org/10.1021/nn500532f.

(23) Zhou, W.; Zou, X.; Najmaei, S.; Liu, Z.; Shi, Y.; Kong, J.; Lou, J.; Ajayan, P. M.; Yakobson, B. I.; Idrobo, J. C. Intrinsic Structural Defects in Monolayer Molybdenum Disulfide. *Nano Lett.* **2013**, *13*, 2615–2622. https://doi.org/10.1021/nl4007479.

(24) Bertolazzi, S.; Bonacchi, S.; Nan, G.; Pershin, A.; Beljonne, D.; Samorì, P. Engineering Chemically Active Defects in Monolayer MoS_2 Transistors via Ion-Beam Irradiation and Their Healing via Vapor Deposition of Alkanethiols. *Adv. Mater.* **2017**, *29*. https://doi.org/10.1002/adma.201606760.

(25) Tsai, M. L.; Su, S. H.; Chang, J. K.; Tsai, D. S.; Chen, C. H.; Wu, C. I.; Li, L. J.; Chen, L. J.; He, J. H. Monolayer MoS_2 Heterojunction Solar Cells. *ACS Nano* **2014**, *8*, 8317–8322. https://doi.org/10.1021/nn502776h.

(26) Lee, Y. T.; Kang, J. H.; Kwak, K.; Ahn, J.; Choi, H. T.; Ju, B. K.; Shokouh, S. H.; Im, S.; Park, M. C.; Hwang, D. K. High-Performance 2D MoS_2 Phototransistor for Photo Logic Gate and Image Sensor. *ACS Photonics* **2018**, *5*, 4745–4750. https://doi.org/10.1021/acsphotonics.8b01049.

(27) Ding, Q.; Czech, K. J.; Zhao, Y.; Zhai, J.; Hamers, R. J.; Wright, J. C.; Jin, S. Basal-Plane Ligand Functionalization on Semiconducting 2H-MoS_2 Monolayers. *ACS Appl. Mater. Interfaces* **2017**, *9*, 12734–12742. https://doi.org/10.1021/acsami.7b01262.

(28) Makarova, M.; Okawa, Y.; Aono, M. Selective Adsorption of Thiol Molecules at Sulfur Vacancies on MoS_2(0001), Followed by Vacancy Repair via S-C Dissociation. *J. Phys. Chem. C* **2012**, *116*, 22411–22416. https://doi.org/10.1021/jp307267h.

(29) Chen, X.; Berner, N. C.; Backes, C.; Duesberg, G. S.; McDonald, A. R. Functionalization of Two-Dimensional MoS_2: On the Reaction between MoS_2 and Organic Thiols. *Angew. Chem. Int. Ed.* **2016**, *55*, 5803–5808. https://doi.org/10.1002/anie.201510219.

(30) Ionescu, R.; George, A.; Ruiz, I.; Favors, Z.; Mutlu, Z.; Liu, C.; Ahmed, K.; Wu, R.; Jeong, J. S.; Zavala, L.; *et al.* Oxygen Etching of Thick MoS_2 Films. *Chem. Commun.* **2014**, *50*, 11226–11229. https://doi.org/10.1039/c4cc03911d.

(31) Yamamoto, M.; Einstein, T. L.; Fuhrer, M. S.; Cullen, W. G. Anisotropic Etching of Atomically Thin MoS_2. *J. Phys. Chem. C* **2013**, *117*, 25643–25649. https://doi.org/10.1021/jp410893e.

(32) Wang, L.; Ji, X.; Chen, F.; Zhang, Q. Temperature-Dependent Properties of Monolayer MoS_2 Annealed in an Ar Diluted S Atmosphere: An Experimental and First-Principles Study. *J. Mate. Chem. C* **2017**, *5*, 11138–11143. https://doi.org/10.1039/c7tc03672h.

(33) Dumcenco, D.; Ovchinnikov, D.; Marinov, K.; Lazić, P.; Gibertini, M.; Marzari, N.; Sanchez, O. L.; Kung, Y. C.; Krasnozhon, D.; Chen, M. W.; et al. Large-Area Epitaxial Monolayer MoS_2. *ACS Nano* **2015**, *9*, 4611–4620. https://doi.org/10.1021/acsnano.5b01281.

(34) Lee, Y. H.; Zhang, X. Q.; Zhang, W.; Chang, M. T.; Lin, C. te; Chang, K. di; Yu, Y. C.; Wang, J. T. W.; Chang, C. S.; Li, L. J.; *et al.* Synthesis of Large-Area MoS_2 Atomic Layers with Chemical Vapor Deposition. *Adv. Mater.* **2012**, *24*, 2320–2325. https://doi.org/10.1002/adma.201104798.

(35) Yu, Y.; Li, C.; Liu, Y.; Su, L.; Zhang, Y.; Cao, L. Controlled Scalable Synthesis of Uniform, High-Quality Monolayer and Few-Layer MoS_2 Films. *Sci. Rep.* **2013**, *3*, 1–6. https://doi.org/10.1038/srep01866.

(36) Li, H.; Zhang, Q.; Chong, C.; Yap, R.; Tay, K.; Hang, T.; Edwin, T.; Olivier, A.; Baillargeat, D. From Bulk to Monolayer MoS_2: Evolution of Raman Scattering. *Adv. Funct. Mater.* **2012**, *22*, 1385–1390. https://doi.org/10.1002/adfm.201102111.

(37) Li, Y.; Li, X.; Chen, H.; Shi, J.; Shang, Q.; Zhang, S.; Qiu, X.; Liu, Z.; Zhang, Q.; Xu, H.; *et al.* Controlled Gas Molecules Doping of Monolayer MoS_2 via Atomic-Layer-Deposited Al_2O_3 Films. *ACS Appl. Mater. Interfaces* **2017**, *9*, 27402–27408. https://doi.org/10.1021/acsami.7b08893.

(38) Li, H.; Wu, J.; Huang, X.; Yin, Z.; Liu, J.; Zhang, H. A Universal, Rapid Method for Clean Transfer of Nanostructures onto Various Substrates. *ACS Nano* **2014**, *8*, 6563–6570. https://doi.org/10.1021/nn501779y.

(39) Lien, D. H.; Uddin, S. Z.; Yeh, M.; Amani, M.; Kim, H.; Ager, J. W.; Yablonovitch, E.; Javey, A. Electrical Suppression of All Nonradiative Recombination Pathways in Monolayer Semiconductors. *Science* **2019**, *364*, 468–471. https://doi.org/10.1126/science.aaw8053.

(40) Mak, K. F.; He, K.; Lee, C.; Lee, G. H.; Hone, J.; Heinz, T. F.; Shan, J. Tightly Bound Trions in Monolayer MoS_2. *Nat. Mater.* **2013**, *12*, 207–211. https://doi.org/10.1038/nmat3505.

(41) Li, H.; Zhang, Q.; Duan, X.; Wu, X.; Fan, X.; Zhu, X.; Zhuang, X.; Hu, W.; Zhou, H.; Pan, A.; *et al.* Lateral Growth of Composition Graded Atomic Layer $MoS_{2(1-x)}Se_{2x}$ Nanosheets. *J. Am. Chem. Soc.* **2015**, *137*, 5284–5287. https://doi.org/10.1021/jacs.5b01594.

(42) Tang, D.; Wang, F.; Zhang, B.; Li, Y.; Li, Y.; Feng, Y.; Han, Y.; Ma, J.; Ren, T.; Zhang, K. Field Effect Properties of Single-Layer $MoS_{2(1-x)}Se_{2x}$ Nanosheets Produced by a One-Step CVD Process. *J. Mater. Sci.* **2018**, *53*, 14447–14455. https://doi.org/10.1007/s10853-018-2617-5.

(43) Yanase, T.; Watanabe, S.; Weng, M.; Nagahama, T.; Shimada, T. Chemical Vapor Deposition of MoS_2: Insight into the Growth Mechanism by Separated Gas Flow Experiments. *J. Nanosci. Nanotechnol.* **2016**, *16*, 3223–3227. https://doi.org/10.1166/jnn.2016.12313.

(44) Mengting, W.; Yanase, T.; Uehara, F.; Watanabe, S.; Miura, T.; Nagahama, T.; Shimada, T. Switching of the Products by Changing the Size and Shape of Catalytic Nanoparticles

during CVD Growth of MoS_2 Nanotubes. *CrystEngComm* **2017**, *19*, 3915–3920. https://doi.org/10.1039/c7ce00608j.

(45) Kern, W. The Evolution of Silicon Wafer Cleaning Technology. *J. Electrochem. Soc.* **1990**, 137, 1887–1892. https://doi.org/10.1149/1.2086825.

For Table of Contents Use Only

Healing Sulfur Vacancies in Monolayer MoS_2 by High-Pressure Sulfur and Selenium Annealing

Takashi Yanase, Fumiya Uehara, Itsuki Naito, Taro Nagahama, Toshihiro Shimada